**Title:** Characterization of extracellular vesicles and artificial nanoparticles with four orthogonal single-particle analysis platforms

**Authors:**

Emily R. Mallick[1,#], emilymallick@gmail.com
Tanina Arab[1,#] ORCID 0000-0003-4485-1096, tarab1@jhu.edu
Yiyao Huang[1] ORCID 0000-0003-1749-963X, yiyaohuang@jhu.edu
Liang Dong[2] ORCID 0000-0001-7689-3237, ldong4@jhmi.edu
Zhaohao Liao[1], zliao@jhmi.edu
Zezhou Zhao[1] ORCID 0000-0003-4792-6073, zach.zhao621@gmail.com
Barbara Smith[3], bsmit112@jhmi.edu
Norman J. Haughey[4] ORCID 0000-0001-5194-4122, nhaughe1@jhmi.edu
Kenneth J. Pienta[2] ORCID 0000-0002-4138-2186, kpienta1@jhmi.edu
Barbara S. Slusher[4,5] ORCID 0000-0001-9814-4157, bslusher@jhmi.edu
Patrick M. Tarwater[6] ORCID 0000-0002-6791-1090, tarwater@jhu.edu
Juan Pablo Tosar[7,8] ORCID 0000-0002-2021-2479, jptosar@pasteur.edu.uy
Angela M. Zivkovic[9] ORCID 0000-0002-2828-7862, amzivkovic@ucdavis.edu
Wyatt N. Vreeland[10] ORCID 0000-0003-0524-8403, wyatt.vreeland@nist.gov
Michael E. Paulaitis[11] ORCID 0000-0002-9628-1091, michaelp@jhmi.edu
Kenneth W. Witwer[1,4,*] ORCID 0000-0003-1664-4233, kwitwer1@jhmi.edu

**Author Information:**

[1]Department of Molecular and Comparative Pathobiology, Johns Hopkins University School of Medicine, Baltimore, MD, US
[2]Department of Urology, Johns Hopkins University School of Medicine, Baltimore, MD, US
[3]Department of Cell Biology, Johns Hopkins University School of Medicine, Baltimore, MD, US
[4]Department of Neurology, Johns Hopkins University School of Medicine, Baltimore, MD, US
[5]Johns Hopkins Drug Discovery, Johns Hopkins University School of Medicine, Baltimore, MD
[6]Department of Epidemiology, Johns Hopkins University Bloomberg School of Public Health, Baltimore, MD, US
[7]Faculty of Science, Universidad de la República, Montevideo, Uruguay
[8]Functional Genomics Unit, Institut Pasteur de Montevideo, Montevideo, Uruguay
[9]Department of Nutrition, University of California Davis, Davis, CA, US
[10]Bioprocess Measurement Group, National Institute of Standards and Technology, Gaithersburg, MD, US
[11]Center for Nanomedicine at the Wilmer Eye Institute, Johns Hopkins University School of Medicine, Baltimore, MD, US

[#]These authors contributed equally to this work

***Corresponding Author:**
Kenneth W. Witwer, PhD
733 North Broadway
Miller Research Building, Room 827
Baltimore, MD 21205
Phone: 1-410-955-9770
Fax: 1-410-955-9823
Email: kwitwer1@jhmi.edu

**Keywords:** extracellular vesicles, exosomes, microvesicles, ectosomes, nanoparticle tracking analysis, single particle interferometric reflectance imaging sensing, resistive pulse sensing, nanoflow cytometry

## ABSTRACT

We compared four orthogonal technologies for sizing, counting, and phenotyping of extracellular vesicles (EVs) and synthetic particles. The platforms were: single-particle interferometric reflectance imaging sensing (SP-IRIS) with fluorescence, nanoparticle tracking analysis (NTA) with fluorescence, microfluidic resistive pulse sensing (MRPS), and nanoflow cytometry measurement (NFCM). Results were compared with standard EV characterization techniques such as transmission electron microscopy (TEM) and Western blot (WB). EVs from the human T lymphocyte line H9 (high CD81, low CD63) and the promonocytic line U937 (low CD81, high CD63) were separated from culture conditioned medium (CCM) by differential ultracentrifugation (dUC) or a combination of ultrafiltration (UF) and size exclusion chromatography (SEC) and characterized per MISEV2018 guidelines. Mixtures of synthetic particles (silica and polystyrene spheres) with known sizes and/or concentrations were also tested. MRPS and NFCM returned similar particle counts, while NTA detected counts approximately one order of magnitude lower for EVs, but not for synthetic particles. SP-IRIS events could not be used to estimate particle concentrations. For sizing, SP-IRIS, MRPS, and NFCM returned similar size profiles, with smaller sizes predominating (per power law distribution), but with sensitivity typically dropping off below diameters of 60 nm. NTA detected a population of particles with a mode diameter greater than 100 nm. Additionally, SP-IRIS, MRPS, and NFCM were able to identify at least three of four distinct size populations in a mixture of silica or polystyrene nanoparticles. Finally, for tetraspanin phenotyping, the SP-IRIS platform in fluorescence mode and NFCM were able to detect at least two markers on the same particle. Based on the results of this study, we can draw conclusions about existing single-

79 particle analysis capabilities that may be useful for EV biomarker development and mechanistic
80 studies.
81
82

## INTRODUCTION

Classification of extracellular vesicles (EVs) into subtypes has been proposed based on size, biogenesis pathway, separation procedure, cellular or tissue origin, and function, among others [1–6]. However, reproducible classification of EV subtypes will require single-particle characterization techniques including phenotyping by surface molecules or molecular signatures [7,8]. In this sense, current knowledge of EV subtypes could be compared with knowledge of immune cells in the 1970s and early 1980s. Around that time, multiplexed flow cytometry capabilities and cell sorting were developed, allowing more precise identification, characterization, and molecular and functional profiling of immune cell subsets [9]. Single-particle technologies for much smaller biological entities will be needed to divide heterogeneous EV populations into well-defined and easily recognized subgroups.

In this study, we evaluated several particle types and single-particle characterization platforms. For input, we used a selection of biological and synthetic particles. EVs were separated from culture medium of H9 T lymphocytic cells and U937 promonocytic cells using several methods. These two cell lines were chosen because they display distinct tetraspanin levels. Specifically, H9 have high CD81 and low CD63 levels, while U937 produce little CD81 but abundant CD63. Mixtures of distinct sizes of synthetic silica and polystyrene beads were also tested. The technology platforms (Text Box 1) were: single-particle interferometric reflectance imaging sensing (SP-IRIS, NanoView) [10,11] with fluorescence, nanoparticle tracking analysis (NTA, ParticleMetrix) [12–14] with fluorescence, microfluidic resistive pulse sensing (MRPS, Spectradyne) [14,15], and nanoflow cytometry measurement (NFCM, NanoFCM) [16,17].

106

**Text Box 1: Evaluated Technologies**

Single-particle interferometric reflectance imaging sensing (SP-IRIS) captures particles (*e.g.* EVs) onto a chip by affinity reagents, usually antibodies, to surface antigens. Particles are imaged by interferometric reflectance for sizing and counting, and fluorescence detection may be done for up to three channels for surface antigens or internal molecules following fixation and permeabilization. Website for the platform we used: https://www.nanoviewbio.com/

Nanoparticle tracking analysis (NTA) is an optical method to track single particles and assign sizes and counts. Measuring Brownian motion allows calculation of a hydrodynamic sphere-equivalent radius of each tracked particle. Additionally, fluorescence filters can be used for detection of particle-associated fluorescence moieties channels. Website for the platform we used: https://www.particle-metrix.de/en/particle-metrix

Microfluidic resistive pulse sensing (MRPS) counts and sizes particles as they pass through a pore between microfluidic chambers. Occlusion of the pore results in a measurable change in electrical signal (defining an event) that is proportional to the volume of the particle. Often, this technique uses different disposable cartridge pore sizes to detect particle populations within specific size ranges. As a non-optical technology, fluorescence detection is not available. Website for the platform we used: https://nanoparticleanalyzer.com/

Nanoflow cytometry measurement (NFCM) is a flow-based technique that detects nano-sized particles by scatter and/or fluorescence. Compared with traditional flow cytometry, a smaller flow channel reduces background signal, and lower system pressure increases dwell time of particles for enhanced signal integration. Website for the platform we used: http://www.nanofcm.com/products/flow-nanoanalyzer

107

## MATERIALS AND METHODS

*Please see Table 1 for manufacturer, part number, and (where applicable) dilution of reagents.*

***Certain commercial equipment, instruments, and reagents are identified in this paper to foster understanding. Such identification does not imply recommendation or endorsement by the National Institute of Standards and Technology or any other entity, nor does it imply that the materials or equipment identified are necessarily the best available for the purpose.***

**Particle Preparation:** Human cells lines H9 (T lymphocytic) and U937 (pro-monocytic) were obtained from the American Type Culture Collection (ATCC). Cells were maintained in Roswell Park Memorial Institute (RPMI) 1640 Medium supplemented with either replete or EV-depleted 10% heat-inactivated fetal bovine serum, with 1% HEPES buffer, 1% Penicillin-Streptomycin, and 1% L-Glutamine. Cells were cultured at 37°C in 5% $CO_2$. Silica spheres (SS) were obtained from NanoFCM (Nottingham, England) as a premixed combination of diameters 68 nm, 91 nm, 113 nm, and 151 nm. Individual polystyrene spheres (PS) were purchased at diameters 70 nm, 90 nm, 122 nm, and 152 nm. Equal concentrations ($1 \times 10^{12}$ particles/mL) of beads were mixed.

**Size Exclusion Chromatography (SEC):** 60 mL of conditioned culture medium (CCM) from each cell line was centrifuged at 1,000 × g for 5 minutes at 4°C to remove cells and cellular debris. 3 kDa molecular weight cut off (MWCO) Centricon Plus-70 centrifugal filters (Millipore Sigma) were used to concentrate the initial volume to 1.5 mL. Size exclusion chromatography (SEC) was done with qEV Automated Fraction Collectors (AFC; Izon Science, Cambridge, MA) and qEV original 70 nm columns (Izon Science, Cambridge, MA). Columns were left at room

131 temperature for 30 minutes and washed with phosphate-buffered saline (PBS). EVs were loaded
132 onto the column, and 0.5 mL fractions were collected by adding additional PBS to the column.
133 EV enriched fractions (SEC; fractions 7-9) were pooled and further concentrated using 3 kDa
134 MWCO Amicon Ultra-15 Centrifugal Filters to a final volume of 1 mL. 50 µL aliquots were
135 stored at -20°C for downstream assays.
136
137 **Differential Ultracentrifugation (dUC):** 60 mL of CCM from each cell line was centrifuged at
138 1,000 × g for 5 minutes at 4°C to remove cells and cellular debris and 2,000 × g for 10 minutes at
139 4°C to remove additional debris. The supernatant was transferred to polypropylene thin-wall
140 ultracentrifugation (UC) tubes and centrifuged at 10,000 × g for 30 minutes at 4°C using a
141 swinging bucket rotor (Thermo Scientific rotor model AH-629, k-factor 242, acceleration and
142 deceleration settings of 9) to pellet large EVs. Supernatant was transferred into new
143 polypropylene thin wall UC tubes and centrifuged at 100,000 × g for 70 minutes at 4°C using the
144 same swinging bucket rotor. The 100K pellets containing small EVs were resuspended in 1 mL
145 of PBS, vigorously vortexed, and placed on ice for 20 minutes. 50 µL aliquots were stored at -
146 20°C for downstream assays.
147
148 **Transmission Electron Microscopy (TEM)**: 10 µL freshly thawed aliquots were adsorbed to
149 glow-discharged carbon-coated 400 mesh copper grids by flotation for 2 minutes. Grids were
150 quickly blotted and rinsed by flotation on 3 drops (1 minute each) of 1× Tris-buffered saline.
151 Grids were negatively stained in 2 consecutive drops of 1% uranyl acetate (UAT)
152 with tylose (1% UAT in deionized water ($dIH_2O$), double filtered through a 0.22 µm filter),
153 blotted, then quickly aspirated to cover the sample with a thin layer of stain. Grids were imaged

154 on a Hitachi 7600 TEM operating at 80 kV with an AMT XR80 CCD (8 megapixel). SS and PS
155 were absorbed to grids as above, but with initial flotation for 5 minutes and imaging on a Phillips
156 CM-120 TEM operating at 80 kV with an AMT XR80 CCD (8 megapixel).
157
158 **Western Blot (WB):** H9 and U937 cell pellets and isolated EVs were lysed in 1×
159 radioimmunoprecipitation assay buffer (RIPA) supplemented with protease inhibitor cocktail.
160 Protein quantification of cell and EV lysates was done using a bicinchoninic acid assay (BCA)
161 (Pierce BCA Protein Assay Kit). 5 µg of lysates were resolved using a 4% to 15% Criterion
162 TGX Stain-Free Precast gel, then transferred onto an Immuno-Blot PVDF membrane. Blots were
163 probed using primary antibodies in PBS-T and 5% Blotting Grade Blocker. Primary antibodies
164 included anti-CD81, anti-CD63, anti-CD9, anti-TSG101, anti-BiP/GRP78, and anti-GM130.
165 Rabbit anti-mouse IgGk BP-HRP and Mouse anti-rabbit IgGk BP-HRP were used as secondary
166 antibodies. SuperSignal West Pico PLUS Chemiluminescent Substrate was used for detection
167 and blots were visualized with an iBright Western Blot (Thermo Fisher, Waltham, MA) imaging
168 system.
169
170 **Single Particle Interferometric Reflectance Imaging (SP-IRIS):** Measurements were
171 performed largely as described previously [18,19]. 35 µL of H9 and U937 EVs isolated by SEC
172 or dUC were diluted 1:1 in incubation buffer (IB) and incubated at room temperature
173 on ExoView R100 (NanoView Biosciences, Brighton, MA) chips printed with anti-human CD81
174 (JS-81), anti-human CD63 (H5C6), anti-human CD9 (HI9a), and anti-mouse IgG1 (MOPC-21).
175 After incubation for 16 hours, chips were washed with IB 4 times for 3 minutes each under
176 gentle horizontal agitation at 500 rpm. Chips were then incubated for 1 hour at room temperature

with a fluorescent antibody cocktail of anti-human CD81 (JS-81, CF555), anti-human CD63 (H5C6, CF647), and anti-human CD9 (HI9a, CF488A) at a dilution of 1:1200 (v:v) in a 1:1 (v:v) mixture of IB and blocking buffer. The buffer was then exchanged to IB only, followed by 1 wash with IB, 3 washes with wash buffer, and 1 wash with rinse buffer (3 minutes each at 500 rpm). Chips were immersed twice in rinse buffer for approximately 5 seconds each and removed at a 45-degree angle to allow the liquid to vacate the chip. All reagents and antibodies were supplied by NanoView Biosciences (Brighton, MA, Cat #EV-TETRA-C). Both SS and PS were diluted in $dIH_2O$ to load 10,000 particles, nominally, per antibody capture spot on the ExoView chips. 35 µL of diluted spheres were incubated on ExoView chips and allowed to fully dry. All chips were imaged in the ExoView scanner (NanoView Biosciences, Brighton, MA) by interferometric reflectance imaging and fluorescent detection. Data were analyzed using NanoViewer 2.8.10 Software (NanoView Biosciences). Fluorescent cutoffs were as follows: CF555 channel 230, CF488 channel 475, CF647 channel 250 (biological particles) and CF555 channel 675, CF488 channel 600, and CF647 channel 375 (SS and PS).

**Nanoparticle Tracking Analysis (NTA):** ZetaView QUATT-NTA Nanoparticle Tracking-Video Microscope PMX-420 and BASIC NTA-Nanoparticle Tracking Video Microscope PMX-120 (Particle Metrix, Inning am Ammersee, Germany) instruments were used for particle quantification in both scatter and fluorescence (488 nm) modes. All calibration beads were diluted using distilled water, and all samples were diluted in PBS to a final volume of 1 mL. Calibration was done for both scatter and fluorescence measurements. For scatter-mode calibration, 100 nm PS were diluted 1:250,000 (v:v). Capture settings were: sensitivity 65, shutter 100, minimum trace length 10. Cell temperature was maintained at 25°C for all

measurements. For fluorescence calibration, 488 nm yellow-green FluoSpheres were diluted 1:250,000 (v:v), and both scatter and fluorescence were measured. Scatter was recorded as above, and fluorescence was measured at sensitivity 80, shutter 100, and minimum trace length 15. For H9 and U937 EVs isolated by SEC or dUC, one cycle was performed by scanning 11 cell positions. Capture was done at medium video setting corresponding to 30 frames per position. PE-conjugated mouse anti-human CD81 and AF488-conjugated mouse anti-human CD63 were used for fluorescence detection of EVs. Antibodies were mixed 1:9 (v:v) with PBS, incubated 2 hours at room temperature, and diluted to a final volume of 1 mL. For SS and PS mixtures, samples were diluted such that at least 200 particles could be counted per frame. Technical triplicates were measured for each sample. A washing step was done between each measurement using $dIH_2O$. ZetaView Software 8.5.10 was used to analyze the recorded videos with the following settings: minimum brightness 30, maximum brightness 255, minimum area 10, and maximum area 1000. Supplementary Table 1 lists all antibodies tested with this platform.

**Microfluidic Resistive Pulse Sensing (MRPS):** Microfluidics resistive pulse sensing measurements were conducted using the nCS1 instrument (Spectradyne, Torrance, CA) as described previously [18]. Sample volumes of a few µL of H9 and U937 EVs isolated by SEC or dUC were diluted with an equal volume of 1% polysorbate 20 (Tween 20) in 1× PBS (PBST) and further diluted with 1× PBS, and loaded onto polydimethylsiloxane cartridges (diameter range 65 nm to 400 nm). Approximately 5 µL of the diluted sample was used and about 25,000 events were recorded for each analyte. SS and PS were diluted 100-fold by volume in $dIH_2O$, then 10-fold by volume with equal volumes of PBST and the remainder with 1× PBS and loaded onto TS-400 polydimethylsiloxane cartridges. Approximately 3,000 events were obtained for

each SS and PS repeat. All acquired results were analyzed using the nCS1 Data Analyzer (Spectradyne, Torrance, CA). For all samples, user-defined filtering was applied by defining 2D polygonal boundaries based on transition time and diameter to exclude false positive signals, similar to gating commonly used in analyzing flow cytometry data.

**Nano-Flow Cytometry Measurement (NFCM):** The nFCM flow nano-Analyzer was used to measure concentration and size of particles following the manufacturer's instructions and as described previously [20]. Briefly, two single photon-counting avalanche photodiodes (APDs) were used for the simultaneous detection of side scatter (SSC) and fluorescence of individual particles. The instrument was calibrated separately for concentration and size using 200 nm PE- and AF488 fluorophore-conjugated PS beads and a Silica Nanosphere Cocktail, respectively. 20 µL of each EV preparation was incubated with 20 µL PE-conjugated CD81 and 5 µL AF488-conjugated CD63 antibodies at 37°C for 30 minutes. After incubation, the mixture was washed twice with PBS and centrifuged at 110,000 × g for 70 min at 4°C (TH-641 rotor, k-factor 114, Thermo Fisher, using thin-wall polypropylene tubes with 13.2 ml capacity and acceleration and deceleration settings of 9). The pellet was resuspended in 50 µL PBS. Events were recorded for 1 minute. Using the calibration curve, the flow rate and side scattering intensity were converted into corresponding particle concentrations and size.

244 **Table 1**

| **Antibodies** | **Manufacturer** | **Cat #** | **Dilution** |
|---|---|---|---|
| Primary Anti-CD81 | Santa Cruz, Dallas, TX | sc-7637 | 1:500 |
| Primary Anti-CD63 | BD Pharmigen, San Diego, CA | 556019 | 1:1000 |
| Primary Anti-CD9 | BioLegend, San Diego, CA | 312102 | 1:1000 |
| Primary Anti-TSG101 | AbCam, Cambridge, MA | ab125011 | 1:1000 |
| Primary Anti-BiP/GRP78 | BD Pharmigen, San Diego, CA | 619078 | 1:500 |
| Primary Anti-GM130 | AbCam, Cambridge, MA | ab52649 | 1:400 |
| Secondary Mouse Anti-Rabbit IgG BP-HRP | Santa Cruz, Dallas, TX | sc-2357 | 1:5000 |
| Secondary Rabbit Anti-Mouse IgGk BP-HRP | Santa Cruz, Dallas, TX | 516102 | 1:5000 |
| PE-Conjugated Mouse Anti-Human CD81 | BD Biosciences, Franklin Lakes, NJ | 555676 | n/a |
| AF488-Conjugated Mouse Anti-Human CD63 | Novus Biologicals, Littleton, CO | NBP2-42225 | n/a |
| **Reagents** | **Manufacturer** | **Cat #** | |
| 3K MWCO Centricon Plus-70 | Millipore Sigma | UFC700308 | |
| 3K MWCO Amicon Ultra-15 | Millipore Sigma | UFC900396 | |
| Blotting Grade Blocker | Bio-Rad | 170-6404 | |
| Carbon Coated 400 Mesh Copper Grids | Electron Microscopy Science | CF400-Cu-UL | |
| Criterion TGX Stain-Free Precast Gel | Bio-Rad | 5678084 | |
| Distilled Water | Gibco | 15230-162 | |
| FluoSpheres Carboxylate-Modified Microspheres, 0.1 µm, Yellow Green Fluorescent | Thermo Scientific | F8803 | |
| H9 Cell Line | American Type Culture Collection | HTB-176 | |
| Heat-Inactivated Fetal Bovine Serum | GE Healthcare | SH30396.03 | |
| Heat-Inactivated Fetal Bovine Serum, Exosome-Depleted | Gibco | A2720801 | |
| HEPES buffer | Gibco | 15630080 | |
| Immuno-Blot PVDF Membrane | Bio-Rad | 1620177 | |
| L-Glutamine | Gibco | 25030081 | |
| Open-Top Thin Wall Ultra-Clear Tubes | Beckman Coulter | 344091 | |
| Penicillin-Streptomycin | Gibco | 15140122 | |

| | | |
|---|---|---|
| Phosphatidylserine Beads | NanoFCM | S16M-Exo |
| Phosphate-Buffered Saline (PBS) | Gibco | 14190-144 |
| Pierce BCA Protein Assay Kit | Thermo Scientific | 23225 |
| Polypropylene Ultracentrifugation (UC) Tubes | Sorvall | 03-141 |
| Polystyrene Spheres 147 nm | Thermo Scientific | 3150A |
| Polystyrene Spheres 125 nm | Thermo Scientific | 3125A |
| Polystyrene Spheres 100 nm | Thermo Scientific | 3100A |
| Polystyrene Spheres 70 nm | Thermo Scientific | 3070A |
| Polystyrene Spheres 90 nm | Thermo Scientific | 3090A |
| Protease Inhibitor Cocktail | Millipore Sigma | 11697498001 |
| RIPA | Cell Signaling Technology | 9806 |
| Roswell Park Memorial Institute (RPMI) 640 Medium | Gibco | 11875093 |
| Silica Nanosphere Cocktail | NanoFCM | n/a |
| SuperSignal West Pico PLUS Chemiluminescent Substrate | Thermo Scientific | 34577 |
| Swinging Bucket Rotor AH-629 | Thermo Scientific | 54284 |
| Tris Buffered Saline (TBS) | Bio-Rad | 1706435 |
| Tween-20 | Millipore Sigma | P7949 |
| U937 Cell Line | American Type Culture Collection | CRL-1593.2 |
| Ultra-Pure Distilled Water | Invitrogen | 10977015 |
| Uranyl Acetate | Polysciences | 2144725 |

## RESULTS

### Production, separation, and quality control of input materials

Supernatants were collected from cultured human cell lines: H9 (T-lymphocytic) and U937 (pro-monocytic). EVs were separated by size exclusion chromatography and ultrafiltration or differential ultracentrifugation (Figure 1A). Marker expression and morphology were assessed by WB (Figure 1B and Supplementary Figure 1) and TEM. WB revealed characteristic CD63 and CD81 expression patterns, with CD81 above the limit of detection only for H9 (Figure 1B). Heterogeneous EV populations were observed by TEM in each sample preparation method (Figure 1C). Additionally, we confirmed size and purity of silica spheres and polystyrene spheres using TEM (Figure 1D).

### Artificial nanoparticle sizing

Mixed silica spheres (SS) with nominal diameters of 68 nm, 91 nm, 113 nm, and 151 nm were measured with the four platforms. Please note that since the SP-IRIS technology uses affinity to capture particles, we dried particle mixtures onto the surface of the SP-IRIS chips before imaging. SP-IRIS identified four distinct populations with diameter modes around 75 nm, 100 nm, 120 nm, and 150 nm (Figure 2A). NTA detected a broad population distribution with a mode around 105 nm diameter (Figure 2B). MRPS resolved four distinct peaks for each individual chip, but this distinction was masked somewhat by averaging all results (Figure 2C; see also Supplementary Figure 2). NFCM resolved four populations with distinct peaks at diameters of approximately 66 nm, 85 nm, 112 nm, and 154 nm (Figure 2D). Polystyrene spheres (PS) with nominal diameters 70 nm, 90 nm, 122 nm, and 152 nm were mixed to a nominal concentration of $1\times10^{12}$ particles/mL. SP-IRIS detected four distinct peaks around 80 nm, 110 nm, 140 nm, and

170 nm (Figure 2E). NTA returned a broad population distribution centered around 105 nm (Figure 2F). MRPS identified distinct peaks at diameters 71 nm, 92 nm, 123 nm, and 150 nm (Figure 2G). For PS, nano-flow showed four populations around 85 nm, 120 nm, 170 nm, and 225 nm in diameter, as well as a possible smaller population around 60 nm (Figure 2H).

**Artificial nanoparticle counting**

In addition to particle size, we also assessed counts. For SP-IRIS, a mean of around 3000 SS particles were detected per printed antibody spot (Figure 3A), with no overall differences between groups of antibody spots (*i.e.,* three spots per chip each of three tetraspanins and an isotype control; note that no differences would be expected, since particles were dried onto the chips). However, per-spot events overall ranged from <2000 SS particles per spot to >4500 SS particles per spot (Figure 3A). SP-IRIS performed similarly for PS. There were no differences between antibody groups, with a mean of around 1400 events/antibody spot (Figure 3B), but events per spot ranged from <1000 PS particles/spot to 3000 PS particles/spot. Interestingly, based on the nominal PS bead concentration and the surface area of the chips and spots, 10,000 particles per spot would be expected (Figure 3B, dotted line). Following SP-IRIS measurements, chips were probed with three fluorescently labeled antibodies (anti-CD81, anti-CD63, and anti-CD9) to assess background binding. Background binding was negligible for both SS and PS (Supplementary Figure 3A and B, respectively). Some outliers were observed for CD9 (SS) or CD63 (PS); however, none exceeded 1000 events. Particle concentrations were also measured by NTA, MRPS, and NFCM. For SS (Figure 3C), MRPS estimated a concentration approximately one log higher than NTA ($5.1\times10^{11}$ particles/mL *vs*. $5.4\times10^{10}$ particles/mL, respectively), with NFCM in the middle ($1.7\times10^{11}$ particles/mL). For PS, all three methods were in close agreement

296 (Figure 3D). Furthermore, the measured concentration was very close to the nominal PS
297 concentration of $1\times10^{12}$ particles/mL (Figure 3D, dotted line).
298
299 **Biological particle sizing**
300 EV preparations from H9 and U937 cell supernatants enriched by ultrafiltration and SEC (SEC
301 EVs) or by differential ultracentrifugation (100K EVs) were next measured using each platform.
302 For H9-derived materials, SP-IRIS returned an almost identical size distribution profile for both
303 EV enrichment methods (Figure 4A). In contrast, NTA, MRPS, and NFCM measured more
304 particles at smaller diameters for the 100K EVs compared with the SEC EVs with roughly
305 similar particle size distributions (Figure 4B-D). However, substantial variation between
306 replicates might limit the conclusions that can be drawn from this observation. For U937-derived
307 materials, SP-IRIS and NTA (Figure 4E,F) detected more particles at smaller diameters from the
308 100K EVs compared with the SEC-EVs, again with roughly similar particle size distribution.
309 MRPS produced equivalent particle size distribution and particle number between the two
310 enrichment techniques (Figure 4G ). In contrast, NFCM detected a higher particle count of
311 smaller particle diameters from the SEC EVs than the 100K EVs, with the particle size
312 distributions significantly different. Again, variability between replicates limits conclusions.
313 Overall, the results are broadly consistent with the reported power-law size distribution of EVs
314 [21,22] and the expectation that UC pellets may contain non-EV extracellular particles (EPs)
315 around the same size as EVs [1].
316
317 **Biological particle counting**

Particle counts were next assessed. As before, we present the SP-IRIS data separately because this platform does not provide an overall count, but rather a number of events detected on chips printed with antibodies (shown here: to CD81 and to CD63 plus an isotype control). Consistent with protein assay results, SP-IRIS shows that more H9 particles were captured by anti-CD81 than by anti-CD63 (Figure 5A) and that U937 particles could be captured by CD63 capture antibodies and not CD81 capture antibodies (Figure 5B). For the remaining three platforms, which measure overall concentration, several trends were apparent (Figure 5C,D). First, for both the H9 and the U937 source, and for both EV separation methods, data were consistent with the results of SS counting in that NTA, NFCM, and MRPS measurements ordinally ranked from lowest particles/mL to highest particles/mL. Secondly, MRPS and NFCM measured greater particle concentrations for 100K EVs than for SEC EVs (corrected for processing and dilution), although NTA results were similar. Finally, this is in contrast to results for the PS particles, where the three techniques produced equivalent particle counts.

**Single particle phenotyping by fluorescence**

The SP-IRIS results represent a type of single-particle phenotyping since diameter is measured for individual particles captured by antibodies and thus putatively positive for an antigen. Captured particles can additionally be probed with fluorescently labeled antibodies. For chips incubated with H9 EVs (Figure 6A,B), EVs captured by CD81 were generally positive for CD81 by fluorescence, and many also appeared to be CD63 positive. In contrast, CD63 capture spots were largely devoid of fluorescence, as were (most) control capture spots. For chips incubated with U937 EVs (Figure 6C,D), events on CD63 capture spots were also positive for CD63 by fluorescence. CD81-linked fluorescence was at background levels for all spots. Note that numbers of "positive" events are higher in fluorescence mode than with SP-IRIS (Figure 5A,B),

likely, as discussed later, because fluorescence detection is more sensitive than reflectance imaging.

For the two remaining platforms with fluorescence capabilities, NTA and NFCM, results are shown as percent of total particles (Figure 6E-H). Approximately 40% to 50% of detected particles from H9 cells were positive for CD81 according to fluorescent NTA, while little to no CD81 signal was detected for U937 materials, consistent with protein assay results. However, we could not detect CD63-linked signal by fluorescent NTA for any sample. In contrast, NFCM detected either CD81 or CD63 on a small percentage of particles. The percentages were similar for the two tetraspanins for H9-derived particles. For U937 material, CD63-positive particles were more abundant than CD81-positive particles. No major differences between the SEC and 100K separation methods were apparent according to these data (Figure 6E-H).

## DISCUSSION

This study evaluated the abilities of four orthogonal technology platforms to size, count, and/or phenotype biological EVs and synthetic nanoparticles. Three of the technologies—SP-IRIS, NTA, and NFCM—are optical in nature and can perform some form of phenotyping/fluorescence analysis, while the other, MRPS, is an electric sensing platform that we did not attempt to apply to particle phenotyping. Although numerous comparisons of EV characterization platforms have been published previously [15,23–26], this study includes NFCM and MRPS and focuses in part on single-particle phenotyping.

***Detected particles: size-range sensitivity and refractive index matter.*** Whereas NTA, MRPS, and NFCM accurately and consistently measured the concentration of a known mixture of polystyrene particles, estimates of the number of silica particles varied substantially. NTA measured approximately 10-fold fewer SS particles than MRPS, while NFCM measured ~ 3-fold fewer SS particles than MRPS. Since SS have a lower refractive index ($n_{SS} \sim 1.42$ [27]) than PS ($n_{PS} \sim 1.59$ [28]), one might predict that a mixture of EVs, with an even lower refractive index than silica [23,29], would have an even larger range of measurements. Indeed, for EV preparations, average counts by NTA and MRPS varied by between one and two orders of magnitude. These outcomes emphasize that each platform has an effective range of measurement that may change with properties of particle populations, especially refractive index. Thus, differences in output in part reflect different or overlapping particle populations that can be detected by the specific technologies, as indeed reported previously for several of these technologies [30]. That is, NTA and MRPS are similarly capable to detect a wide range of PS particle sizes. However, NTA may detect a more limited range of biological particles [31] than

379 the MRPS platform using a small pore-size cartridge, in that MRPS may detect more of the
380 smaller EVs along the power-law distribution. Signal for NTA scales with radius to the $6^{th}$
381 power, whereas signal scales for MRPS with radius to the $3^{rd}$ power; thus, because of finite
382 dynamic range, NTA will be biased to detecting fewer of the small particles in a sample
383 compared with MRPS.
384
385 ***Is it important to resolve different particle size populations?*** SP-IRIS, MRPS, and NFCM could
386 resolve up to four populations of synthetic nanoparticles with different diameters. We note that
387 distinct populations were somewhat obscured when MRPS results were averaged for SS, but not
388 for PS – see Supplementary Figure 4 – which may reflect aggregation of the SS due to the
389 electrolyte solution (PBS) required for MRPS and the convolution of experimental uncertainties
390 in particle concentration and size measurements. Also noteworthy is that the NFCM platform
391 distinguished subpopulations of SS particles, but that this is likely because the same beads are
392 used to calibrate the instrument. While detecting the expected concentration of high refractive
393 index PS particles, NTA was unable to resolve individual particle populations and instead
394 characterized the SS particles as a broad population distribution centered on an "average" size.
395 To be sure, it may be possible to resolve discretely sized particle populations using NTA with
396 mixtures at different ratios of sizes. We could not do so with the mixtures we used. Whether this
397 matters for biological particles is unclear. It does not seem that biological samples would contain
398 unique EV subpopulations with exquisitely defined sizes, except perhaps for samples from
399 sources infected with specific enveloped viruses. NTA does seem to be capable of detecting
400 shifts in population distributions, and this capability might be more important for biological
401 particles than resolving subpopulations.

***On counting by SP-IRIS/fluorescence.*** One clear finding of our study is that, in our hands, neither SP-IRIS label-free measurements nor subsequent fluorescence detection could be used directly to estimate overall particle concentration. Instead, SP-IRIS is best used to understand ratios within populations and for single-particle phenotyping. Even when PS beads were dried onto chips, the measured concentration was approximately one-seventh of the expected concentration. While uneven drying could contribute, it seems that PS particles non-specifically adhered to the chip without a washing step, were undercounted slightly. For biological particles, the problem is compounded since only a subset of EVs bind to any given affinity reagent "spot." Binding is determined by diffusion (which is slow for EVs), presence and density of recognized surface markers, and affinity characteristics of antibody-to-antigen binding. The bound population of particles remaining after wash steps is only a miniscule proportion of the total in the input material and cannot be used to determine overall concentration. Interestingly, fluorescence results often indicated higher particle concentrations than returned by label-free counting, even though particles positive for a particular antigen are expected to be only a subset of the captured population (different antigens) or to approach equality (if the capture antigen is targeted and antigen is abundant). Counts are higher because fluorescence detection is more sensitive than label-free. That is, fluorescence detects positive particles that may be below the limit of label-free detection.

***Did any platforms identify differences between EV separation technologies?*** For both biological sources of EVs, we used two methods of EV separation: dUC (100K EVs), which has been the most common method for EV separation [32,33], and a combination of filtration and

size exclusion chromatography (SEC EVs) [34,35]. According to some evidence in the literature, dUC leads to more protein contamination and aggregation and damage of EVs [36–38]. It should be noted that alternative viewpoints can also be found [16]. However, protein particle contamination might be expected to introduce more and smaller particles. This outcome is indeed observed based upon TEM background and particle profile shifts towards smaller particles for several of the platforms. For SP-IRIS with fluorescence, it is also interesting that tetraspanin positivity is higher for samples obtained by SEC than with dUC. On the other hand, evidence of aggregation by dUC is not apparent in the data presented here. We cannot rule out aggregation, however, only that the techniques used here did not appear to detect it.

***Single-particle phenotyping.*** For the three techniques with single-particle phenotyping capabilities (SP-IRIS, NTA, and NFCM), each has advantages and drawbacks, as covered above, all can potentially provide true single-particle phenotyping data. SP-IRIS was able to achieve the most "multiplexed" detection, in that signal could be obtained above background for up to three fluorescent channels. At the time of our evaluations, the NTA platform we used could not perform simultaneous multi-channel measurements and thus was not a true single-particle multiplexing platform. Instead, sequential filter switches were required, such that the same particles could not be tracked in different channels.

In Table 2, we attempt to summarize our findings and views about the four investigated techniques. **Detectable size ranges** for biological particles: these should be considered to be rough estimates. If we accept the assumption that EVs follow a power-law size distribution (the smaller, the more abundant, with lower bounds defined by membrane curvature constraints), then

no evaluated platform effectively detects the very smallest particles. However, SP-IRIS, MRPS, and NFCM appear to detect slightly smaller particles than NTA under the conditions and settings we tested. For NTA, MRPS, and NFCM, linear ranges for **particle concentration** for all instruments begin around $1\times10^7$ particles/mL and extend from about one order of magnitude (NTA) to multiple orders of magnitude (MRPS). This spread is important, since the wider the range, the fewer time-consuming concentrations or dilutions must be done to place an unknown particle population into the measurable range. SP-IRIS is a special case, since particles are captured by affinity, and overall concentration cannot easily be estimated. In our hands, particle concentrations must be high ($>>1\times10^7$ particles /mL) even for abundant antigens. Furthermore, the optimal captured particle counts are roughly 3000 to 6000 per antibody spot (although this may vary). To hit a very tight "sweet spot", many trial dilutions may be needed. Furthermore, the optimal dilution may well be different for different antibodies on the chip because of different percentages of EVs positive for a particular antigen, per-EV antigen abundance, and antibody performance. Hence, dilutions are usually most important and time-consuming for SP-IRIS. Related to dilution is the **volume of input material** required for a single reading. Assuming each platform can measure $1\times10^7$ particles per mL, the required volume of a dilution at this concentration ranges from 5 ul (MRPS) to around 1 mL (NTA). Of course, the actual volume/number of EVs needed will also depend on the number of concentrations/dilutions required to reach the measurable concentration range. The input volume difference is also inconsequential for highly abundant materials, but may be important for low-abundance EV samples. **If done, optional calibration steps** are rapid for NTA and MRPS (around 20 minutes). For NFCM, we find that calibration can be as short as 20 minutes but can sometimes take longer. Time for sample dilutions is most difficult to estimate, but is expected to correlate inversely with

the range of measurement for each platform. **Read time** ranges from five minute to about half an hour per sample. Note that the times we indicate are for sizing and counting only. Optional fluorescence measurements for the relevant platforms would in some cases add processing time for antibody incubations and removal, as well as for read times (except for NFCM). For SP-IRIS, we should also note that, although the total hands-on and read time is longer than for other techniques, each reading includes on-chip replicates, multiple capture antibodies, and up to three fluorescence readouts per capture antibody.

**Costs** for the platforms include initial outlay, disposable costs, and maintenance costs. For acquisition, the MRPS system is most economical, while NFCM is the most expensive. For basic counting and sizing, operating costs for NTA and NFCM are negligible. Adding optional fluorescence increases these costs by amounts that are antibody-dependent. The MRPS system uses disposable cartridges that currently cost USD 8 to USD 12 each. The SP-IRIS platform has the highest disposable costs, with each sample requiring at least one chip at USD 50 to >USD 100 each. Since optimal dilutions are difficult to achieve and may be different for different capture materials on the same chip, multiple chips may be needed for the same sample. Chips also cannot be chemically stripped and re-used, at least not in our hands (Mallick and Witwer, unpublished data). Furthermore, we find that chips often go unused and are thus "wasted" as a result of a short shelf life of only several weeks. Since chips may take several weeks (or more for custom) to procure, the three-week shelf life requires excellent planning and a lack of unexpected difficulties in the laboratory; otherwise, the investment is wasted. As noted, though, under optimal conditions, the platform provides multi-dimensional information that may justify these costs and logistical challenges for some users. We should also mention that chips for the

494 SP-IRIS and MRPS instruments are currently available only from the instrument manufacturer
495 for that particular measurement technique. As for maintenance costs, we are unable to estimate
496 them at this time.
497
498 **In conclusion:**
499 • No evaluated platform is necessarily "better" or "worse" than others; rather, it is
500 important to be aware of the capabilities of each platform with respect to each particle
501 population of interest.
502 • Rather than relying on a single platform, consider using orthogonal technologies.
503 • Both acquisition and recurring costs should be considered before acquiring a platform.
504 Appropriate reference materials are needed for better evaluation of single particle phenotyping
505 capabilities, including multiplexed phenotyping.
506
507
508

## FIGURE LEGENDS

**Figure 1: Methodology and EV separation.** (A) EVs were isolated from H9 and U937 conditioned cell media by a combination of ultrafiltration and size exclusion chromatography (SEC EVs) or by differential ultracentrifugation (100K EVs). (B) Immunoblot analysis of isolated EVs as well as corresponding cell lysates from H9 and U937 using antibodies specified in Table 1; see also Supplementary Figure 1. (C) Electron microscopy images of SEC EV and 100K EV samples from both cell lines. Leftmost scale bars 500 nm and magnification 40 000×; rightmost scale bars 100 nm and magnification 100 000×. (D) EM of SS and PS. Leftmost scale bars 500 nm and magnification 17 500×; rightmost scale bars 100 nm and magnification 65 000×.

**Figure 2: SS and PS size distribution.** Size distributions for SS (n=3) with standard deviation for (A) SP-IRIS, (B) NTA, (C) MRPS, and (D) NFCM. Nominal SS diameters are at the vertical dotted lines: 68 nm, 91 nm, 113 nm, and 151 nm. Size distributions for PS (n=3; with SD) for (E) SP-IRIS, (F) NTA, (G) MRPS, and (H) NFCM. Nominal PS diameters are at the vertical dotted lines: 70 nm, 90 nm, 122 nm, and 152 nm. Insert in Figure 2C shows a single MRPS measurement of the size distribution.

**Figure 3: SS and PS quantification.** (A) SP-IRIS label-free capture for SS and PS using four capture spots (n=3 per group; mean particle count per spot with SD). B) SS quantification (n=3; mean particles/mL with SD). (C) PS quantification (n=3; mean particles/mL with SD). Nominal PS concentration is portrayed with a horizontal line ($1.0\times10^{12}$ particles/mL).

**Figure 4: H9 and U937 particle size distribution.** Diameters of particles for H9 SEC EVs and 100K EVs (n=3 per group, with standard deviation) for (A) SP-IRIS, (B) NTA, (C) MRPS, and (D) NFCM. Size distributions for U937 SEC EVs and 100K EVs (n=3 per group; with SD) for (E) SP-IRIS, (F) NTA, (G) MRPS, and (H) NFCM.

**Figure 5: H9 and U937 particle quantification.** SP-IRIS label-free capture for (A) H9 SEC EVs and 100K EVs and (B) U937 SEC EVs and 100K EVs using CD81, CD63, and mouse isotype control capture antibodies (n=3 per group; mean particle count/spot with SD). H9 and U937 particle quantification (n=3; mean particles/mL with SD) for (C) SEC EVs and (D) 100K EVs using NTA, MRPS, and NFCM.

**Figure 6: Particle phenotyping.** SP-IRIS fluorescence detection using labeled anti-CD81 and anti-CD63 after particle capture with CD81, CD63, and mouse isotype control (n=3 per group; mean and SD) for (A) H9 SEC EVs, (B) H9 100K EVs, (C) U937 SEC EVs, and (D) U937 100K EVs. Percent of particles detected with fluorescently-labeled anti-CD81 and anti-CD63 by NTA and NFCM (n=3 per group; mean and SD) for (E) H9 SEC EVs, (F) H9 100K EVs, (G) U937 SEC EVs, and (H) U937 100K EVs. Asterisk. An asterisk indicates that, in the authors' view, an antibody did not perform on the instrument; it does not necessarily mean that the antibody would not perform in another context or with additional optimization.

**Supplementary Figure 1: Additional EV characterization.** (A) BCA assay results, including final protein concentrations in µg/mL. (B) Immunoblot analysis of separated EVs as well as corresponding cell lysates from H9 and U937 using antibodies specified in Table 1.

**Supplementary Figure 2: Individual SS measurements by MRPS.** Repeats 2 (A) and 3 (B) for SS using MRPS. Repeat 1 can also be found as an inset in Figure 2C.

**Supplementary Figure 3: SP-IRIS background fluorescence for SS and PS.** SP-IRIS fluorescence detection using fluorescently labeled anti-CD81, anti-CD63, and anti-CD9 after (A) SS and (B) PS capture with four antibody groups (n=3 per group; mean and SD).

**Supplementary Figure 4: MRPS and NFCM dilution series.** SS (A) and PS (B) were diluted 2×, 5×, and 10× by volume to determine the optimal dilution for NTA analysis. SS (C) were diluted 1:1000 (v:v), 1:2000 (v:v), and 1:4000 (v:v) and PS (D) were diluted 1:2500 (v:v), 1:5000 (v:v), and 1:10000 (v:v) to determine the optimal dilution for NFCM analysis. Dilution-corrected counts are for SS (E) and PS (F) on MRPS and SS (G) and PS (H) on NFCM. Optimal dilutions are indicated by green or yellow (MRPS and NFCM, respectively).

**Supplementary Table 1: Antibodies tested with fluorescent NTA.** H9 100K EVs were diluted 1:1 (v:v) in PBS. 9 µL of diluted EVs were mixed with 1 µL of antibody and incubated for 2 hours at room temperature. Samples were then diluted 1:1000 and measured in scatter and fluorescent modes using NTA.

576
577

**Acknowledgements:**

The authors thank members of the Witwer and Retrovirus Laboratories and various members of the International Society for Extracellular Vesicles for discussions and support. The Authors acknowledge NanoView Biosciences, Particle Metrix, Spectradyne, and NanoFCM representatives for discussions and for arranging demonstrations. Electron microscopy images were acquired in the Johns Hopkins University School of Medicine Institute for Basic Biomedical Sciences Microscope Facility.

**Disclosure Statement:**

Authors report no conflicts of interest.

**Funding:**

This work was supported in part by the National Institute on Drug Abuse (NIDA; R01DA040385 and R01DA047807), the National Institute of Mental Health (NIMH; R21MH118164), The National Institute of Allergy and Infectious Diseases (NIAID, R01AI144997), the National Cancer Institute (NCI) and Office of the Director (UG3CA241694) and the Michael J. Fox Foundation (MJFF; Grant 00900821).

# REFERENCES

[1] Théry C, Witwer KW, Aikawa E, et al. Minimal information for studies of extracellular vesicles 2018 (MISEV2018): a position statement of the International Society for Extracellular Vesicles and update of the MISEV2014 guidelines. J Extracell Vesicles 2018;7:1535750.

[2] Yáñez-Mó M, Siljander PR-M, Andreu Z, et al. Biological properties of extracellular vesicles and their physiological functions. J Extracell Vesicles 2015;4:27066.

[3] Witwer KW, Théry C. Extracellular vesicles or exosomes? On primacy, precision, and popularity influencing a choice of nomenclature. J Extracell Vesicles 2019;8:1648167.

[4] Cocucci E, Meldolesi J. Ectosomes and exosomes: shedding the confusion between extracellular vesicles. Trends Cell Biol 2015;25:364–72.

[5] Lázaro-Ibáñez E, Lässer C, Shelke GV, et al. DNA analysis of low- and high-density fractions defines heterogeneous subpopulations of small extracellular vesicles based on their DNA cargo and topology. Https://DoiOrg/101080/2001307820191656993 2019.

[6] Russell AE, Sneider A, Witwer KW, et al. Biological membranes in EV biogenesis, stability, uptake, and cargo transfer: an ISEV position paper arising from the ISEV membranes and EVs workshop. J. Extracell. Vesicles, vol. 8, Taylor and Francis Ltd.; 2019.

[7] Tkach M, Kowal J, Théry C. Why the need and how to approach the functional diversity of extracellular vesicles. Philos Trans R Soc Lond B Biol Sci 2018;373:20160479.

[8] Lässer C, Jang SC, Lötvall J. Subpopulations of extracellular vesicles and their therapeutic potential. Mol Aspects Med 2018;60:1–14.

[9] Lanier LL, Engleman EG, Gatenby P, et al. Correlation of functional properties of human lymphoid cell subsets and surface marker phenotypes using multiparameter analysis and flow cytometry. Immunol Rev 1983;74:143–60.

[10] Reddington AP, Trueb JT, Freedman DS, et al. An Interferometric Reflectance Imaging Sensor for Point of Care Viral Diagnostics. IEEE Trans Biomed Eng 2013;60:3276–83.

[11] Lopez CA, Daaboul GG, Vedula RS, et al. Label-free multiplexed virus detection using spectral reflectance imaging. Biosens Bioelectron 2011;26:3432–7.

[12] Dragovic RA, Gardiner C, Brooks AS, et al. Sizing and phenotyping of cellular vesicles using Nanoparticle Tracking Analysis. Nanomedicine 2011;7:780–8.

[13] Sokolova V, Ludwig AK, Hornung S, et al. Characterisation of exosomes derived from human cells by nanoparticle tracking analysis and scanning electron microscopy. Colloids Surf B Biointerfaces 2011;87:146–50.

[14] Giebel B, Helmbrecht C. Methods to analyze EVs. Methods Mol. Biol., vol. 1545, Humana Press Inc.; 2017, p. 1–20.

[15] Anderson W, Kozak D, Coleman VA, et al. A comparative study of submicron particle sizing platforms: Accuracy, precision and resolution analysis of polydisperse particle size distributions. J Colloid Interface Sci 2013;405:322–30.

[16] Tian Y, Gong M, Hu Y, et al. Quality and efficiency assessment of six extracellular vesicle isolation methods by nano-flow cytometry. J Extracell Vesicles 2020;9.

[17] Tian Y, Ma L, Gong M, et al. Protein Profiling and Sizing of Extracellular Vesicles from Colorectal Cancer Patients via Flow Cytometry. ACS Nano 2018;12:671–80.

[18] Ahn JY, Datta S, Bandeira E, et al. Release of extracellular vesicle miR-494-3p by ARPE-19 cells with impaired mitochondria. Biochim Biophys Acta Gen Subj 2020:129598.

[19] Gámbaro F, Li Calzi M, Fagúndez P, et al. Stable tRNA halves can be sorted into extracellular vesicles and delivered to recipient cells in a concentration-dependent manner. RNA Biol 2019.
[20] Huang Y, Cheng L, Turchinovich A, et al. Influence of species and processing parameters on recovery and content of brain tissue-derived extracellular vesicles. J Extracell Vesicles 2020;9:1785746.
[21] van der Pol E, Böing AN, Gool EL, et al. Recent developments in the nomenclature, presence, isolation, detection and clinical impact of extracellular vesicles. J Thromb Haemost 2016;14:48–56.
[22] Paulaitis M, Agarwal K, Nana-Sinkam P. Dynamic Scaling of Exosome Sizes. Langmuir 2018;34:9387–93.
[23] Van Der Pol E, Coumans FAW, Sturk A, et al. Refractive index determination of nanoparticles in suspension using nanoparticle tracking analysis. Nano Lett 2014;14:6195–201.
[24] Bachurski D, Schuldner M, Nguyen PH, et al. Extracellular vesicle measurements with nanoparticle tracking analysis–An accuracy and repeatability comparison between NanoSight NS300 and ZetaView. J Extracell Vesicles 2019;8.
[25] Erdbrügger U, Lannigan J. Analytical challenges of extracellular vesicle detection: A comparison of different techniques. Cytom Part A 2016;89:123–34.
[26] Corso G, Heusermann W, Trojer D, et al. Systematic characterization of extracellular vesicles sorting domains and quantification at the single molecule–single vesicle level by fluorescence correlation spectroscopy and single particle imaging. J Extracell Vesicles 2019;8.
[27] García-Santamaría F, Míguez H, Ibisate M, et al. Refractive index properties of calcined silica submicrometer spheres. Langmuir 2002;18:1942–4.
[28] Kasarova SN, Sultanova NG, Ivanov CD, et al. Analysis of the dispersion of optical plastic materials. Opt Mater (Amst) 2007;29:1481–90.
[29] Gardiner C, Shaw M, Hole P, et al. Measurement of refractive index by nanoparticle tracking analysis reveals heterogeneity in extracellular vesicles. J Extracell Vesicles 2014;3.
[30] van der Pol E, Coumans FAW, Grootemaat AE, et al. Particle size distribution of exosomes and microvesicles determined by transmission electron microscopy, flow cytometry, nanoparticle tracking analysis, and resistive pulse sensing. J Thromb Haemost 2014;12:1182–92.
[31] Defante AP, Vreeland WN, Benkstein KD, et al. Using Image Attributes to Assure Accurate Particle Size and Count Using Nanoparticle Tracking Analysis. J Pharm Sci 2018;107:1383–91.
[32] Théry C, Amigorena S, Raposo G, et al. Isolation and Characterization of Exosomes from Cell Culture Supernatants and Biological Fluids. Curr. Protoc. Cell Biol., vol. Chapter 3, Hoboken, NJ, USA: John Wiley & Sons, Inc.; 2006, p. Unit 3.22.
[33] Gardiner C, Di Vizio D, Sahoo S, et al. Techniques used for the isolation and characterization of extracellular vesicles: results of a worldwide survey. J Extracell Vesicles 2016;5:32945.
[34] Böing AN, van der Pol E, Grootemaat AE, et al. Single-step isolation of extracellular vesicles by size-exclusion chromatography. J Extracell Vesicles 2014;3:23430.
[35] Théry C, Witwer KW, Aikawa E, et al. Minimal information for studies of extracellular

vesicles 2018 (MISEV2018): a position statement of the International Society for Extracellular Vesicles and update of the MISEV2014 guidelines. J Extracell Vesicles 2019;8:1535750.

[36] Linares R, Tan S, Gounou C, et al. High-speed centrifugation induces aggregation of extracellular vesicles. J Extracell Vesicles 2015;4:29509.

[37] Van Deun J, Mestdagh P, Sormunen R, et al. The impact of disparate isolation methods for extracellular vesicles on downstream RNA profiling. J Extracell Vesicles 2014;3:24858.

[38] Arab T, Raffo-Romero A, Van Camp C, et al. Proteomic characterisation of leech microglia extracellular vesicles (EVs): comparison between differential ultracentrifugation and Optiprep™ density gradient isolation. J Extracell Vesicles 2019;8:1603048.

**Figure 1. Methodology and EV separation**

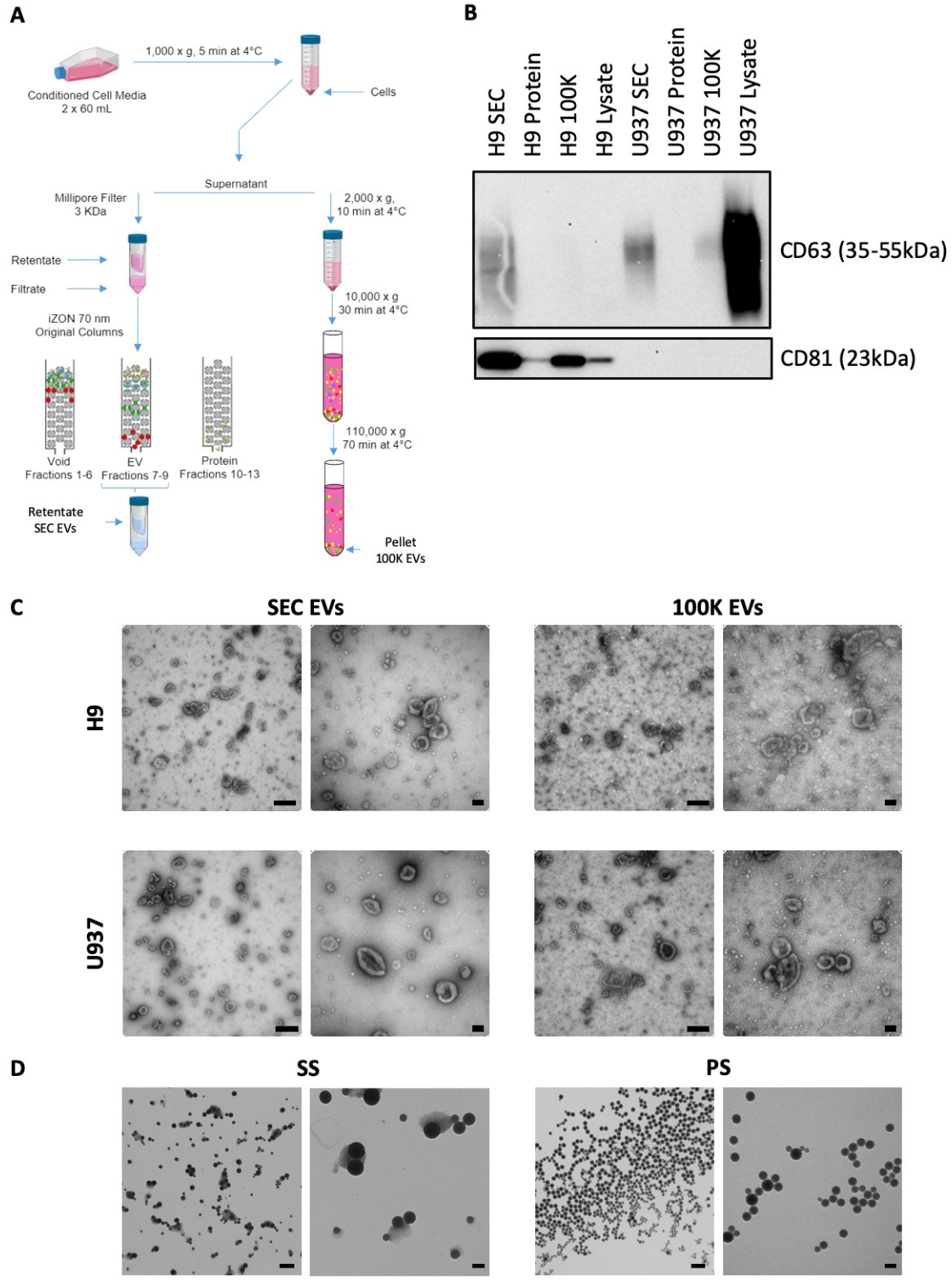


700

**Figure 2. SS and PS size distribution**

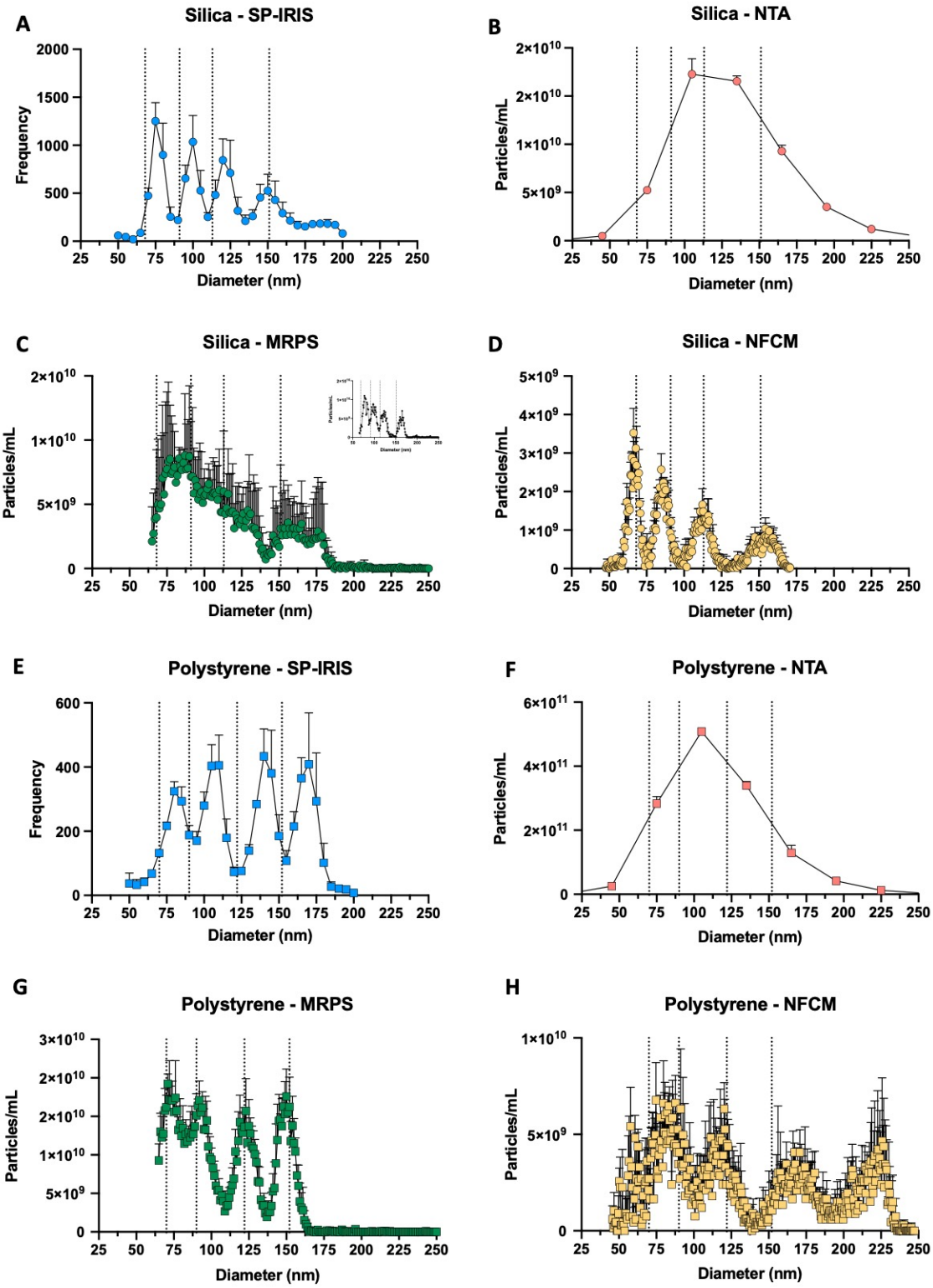


701

**Figure 3. SS and PS quantification**

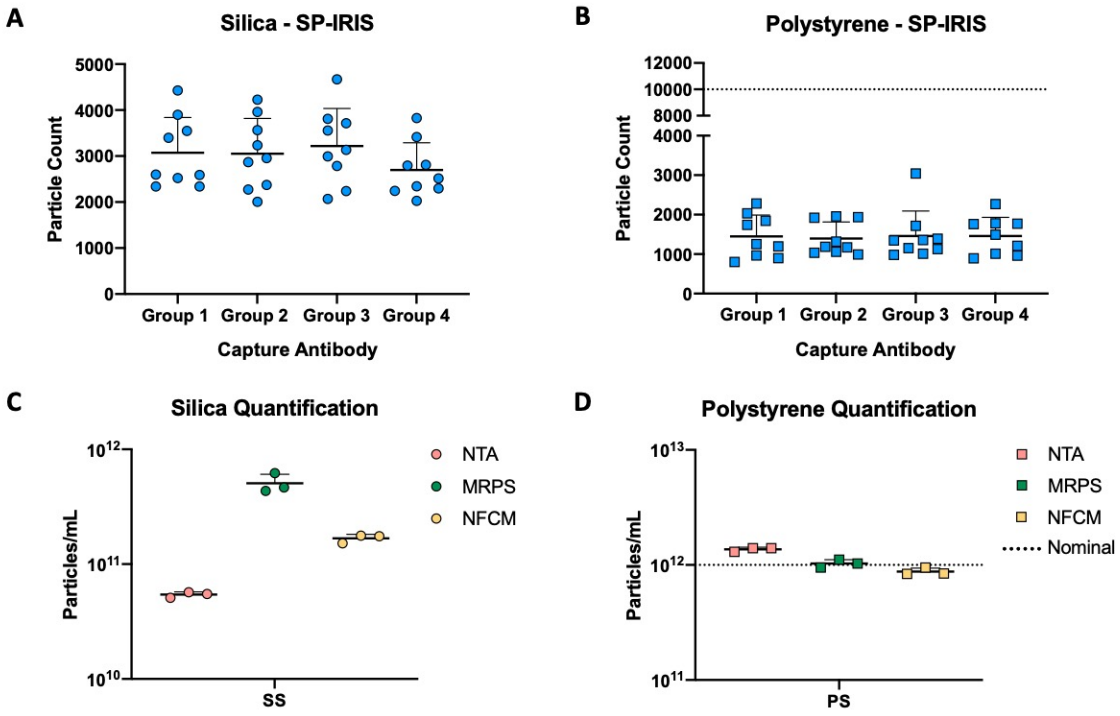


702

**Figure 4. H9 and U937 Size Distribution**

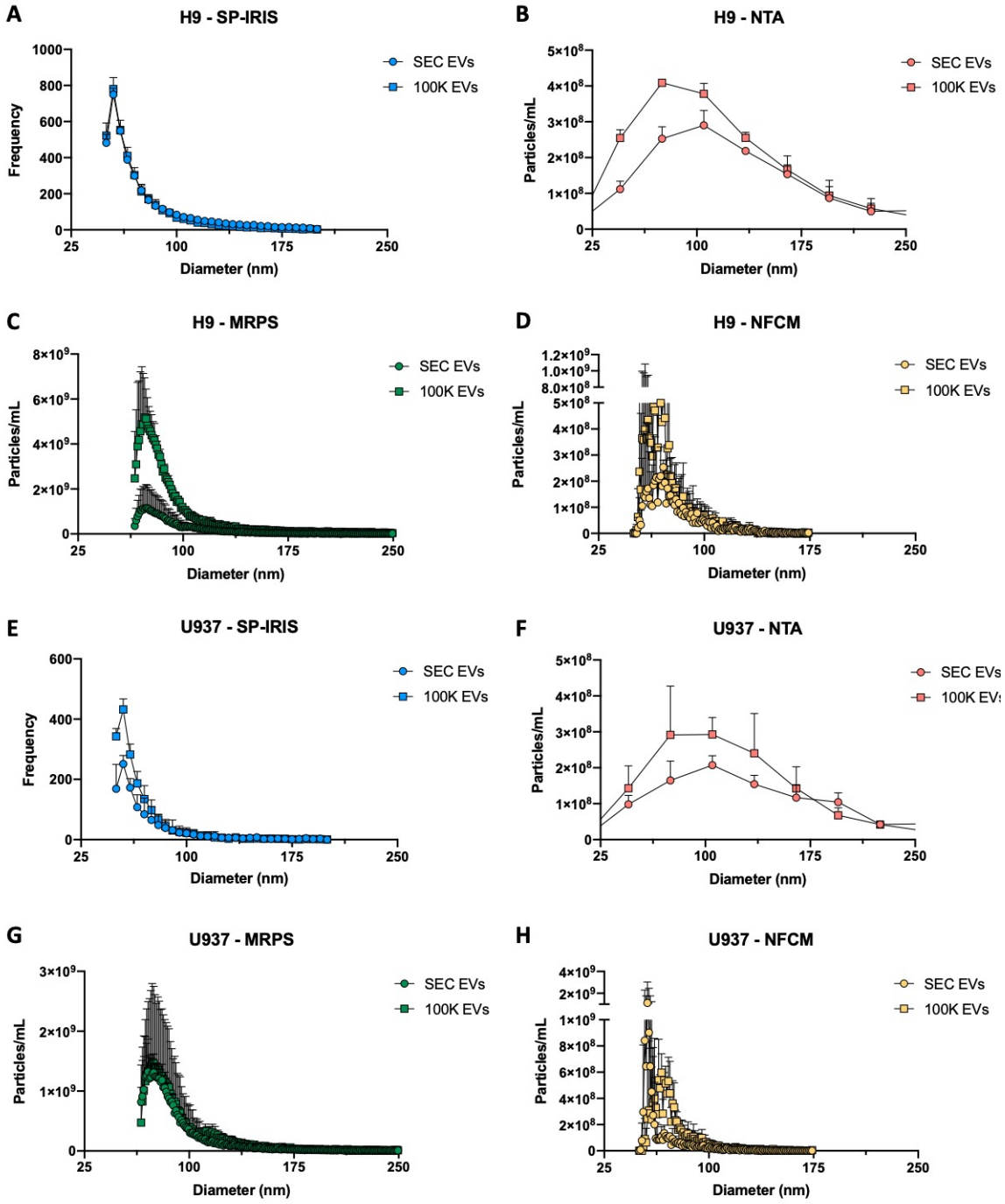


703

**Figure 5. H9 and U937 particle quantification**

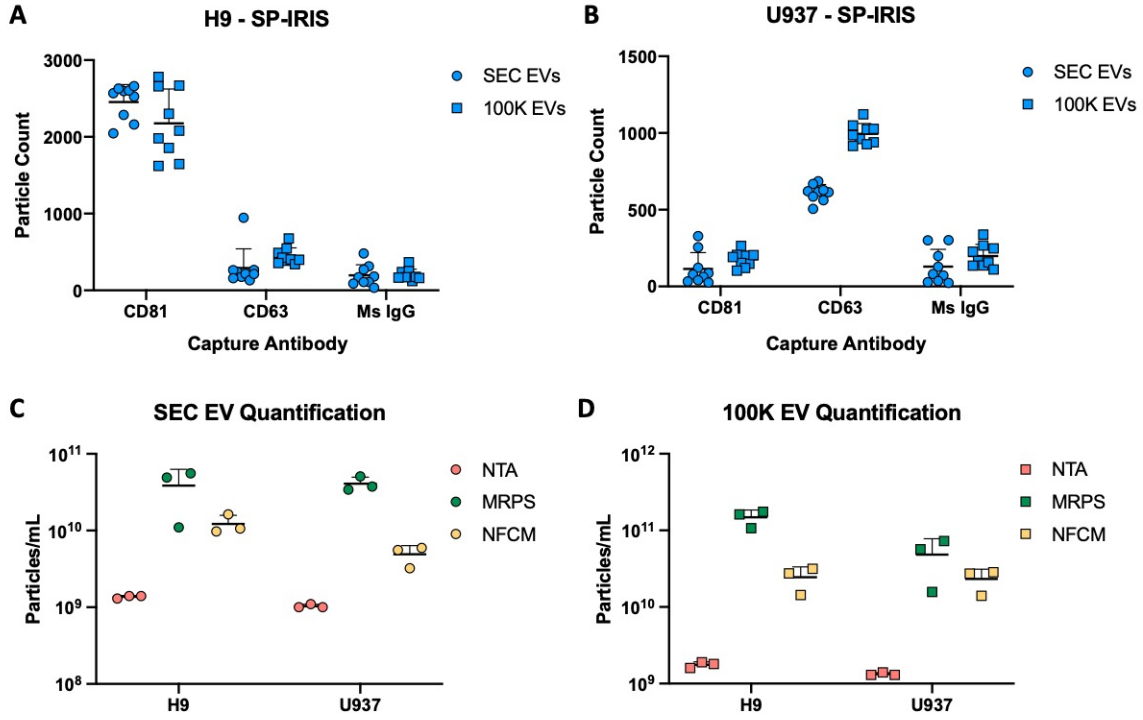


704

**Figure 6. Particle phenotyping**

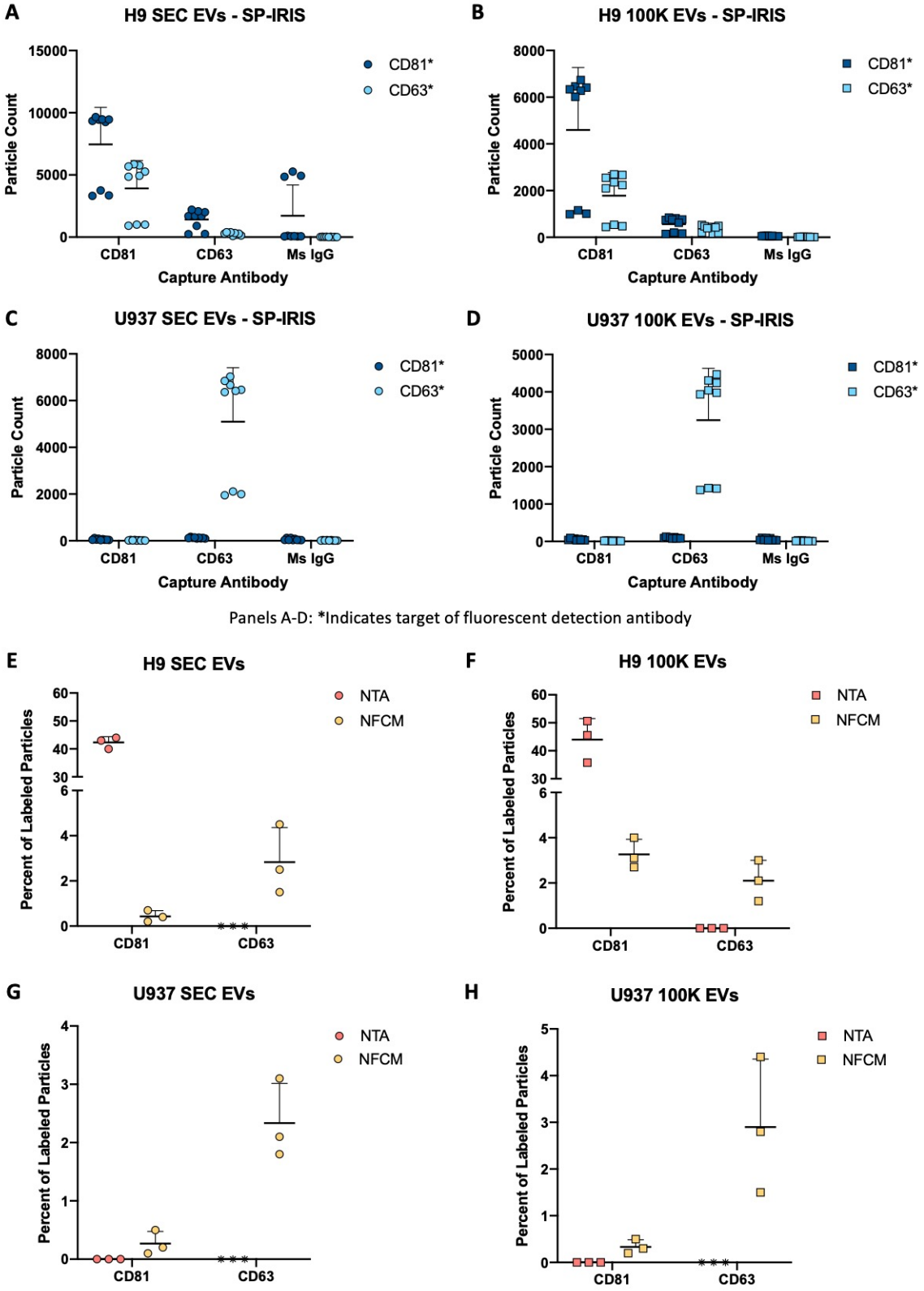


705

## Table 2. Evaluation summary

| Technique | Logistics | | | | | | Performance | | |
|---|---|---|---|---|---|---|---|---|---|
| | Estimated biological particle size detection range (diameter) | Concentration Detection Range | Input volume (µl; may be a dilution) | Operation Time: Hands-on (HO)/ Read time (R) (does not include optional labeling) | Instrument Cost | Costs for disposables | Sizing (including discrimination of different size populations) | Quantification (across all particles, biological and synthetic) | Fluorescence (channels; for instruments we evaluated) |
| SP-IRIS | ~50 nm to 200 nm | n/a; depends on capture Ab, but >>$1\times10^7$ particle/mL preferred | 35 | Day 1: 10 min sample prep (HO) Day 2: 2 hour (HO); 10 min to 30 min per sample (R) | $$ | $$$: Chip/antibody kits (starting at $50/sample to >$100 for custom; ordered from manufacturer) | ++ | - | Up to 3 |
| NTA | ~70 nm to several hundred nm | $1\times10^7$ to $1\times10^8$ particle/mL (in PBS) | 1000 | Optional 20 min calibration (HO/P); 5 min to 15 min per sample (HO/R) | $$ | $: <$1 per sample: 1 mL syringes ($23 per 100, multiple suppliers; Ab not included) | + | + | Up to 4 |
| MRPS | ~50 nm to 2 µm (cartridge-dependent) | $1\times10^7$ to $1\times10^{10}$ particle /mL (in PBS/PBST) | 5 | Optional 20 min calibration (HO/R); 15 min to 30 min per sample (HO/R) | $ | $$: Cartridges ($8 to $12 each, ordered from manufacturer) | ++ | ++ | n/a |
| NFCM | ~40 nm to 170 nm | $1\times10^7$ to $1\times10^9$ particle/mL (in PBS) | 20 | 20 min to 120 min calibration (HO/P); 5 min per sample (HO/P) | $$$ | $: <$1 per sample: 0.5 mL Tubes ($27 per 1000, multiple suppliers; Ab not included) | ++ | ++ | Up to 2 |

RI = refractive index; p/mL = particles per milliliter; Price range: $$$ > $$ > $; values in USD;
Performance indicator: +++ > ++ > + > -

706

**Supplementary Figure 1. Additional EV characterization**

**A**

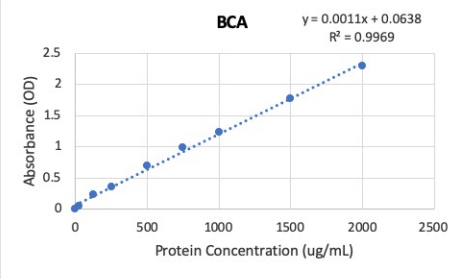


| Sample | Protein Concentration (ug/mL) |
|---|---|
| H9 SEC | 762.42 |
| H9 Protein | 1547.27 |
| H9 100K | 2013.94 |
| H9 Cell lysate | 3941.21 |
| U937 SEC | 550.30 |
| U937 Protein | 1762.42 |
| U937 100K | 1747.27 |
| U937 Cell lysate | 6320.00 |

**B**

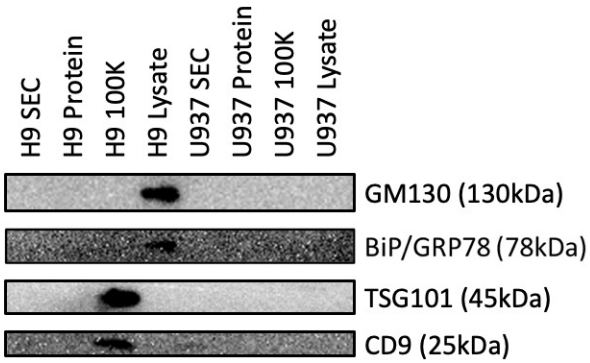

**Supplementary Figure 2. Individual SS measurements by MRPS**

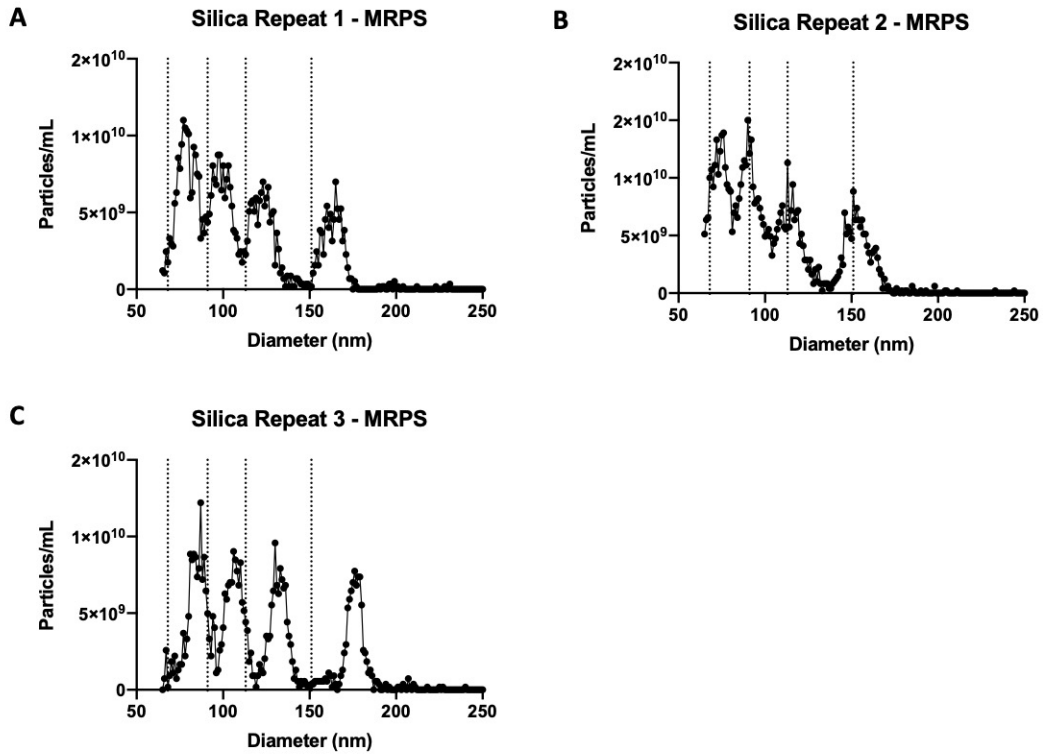


708

**Supplementary Figure 3. SP-IRIS background fluorescence for SS and PS**

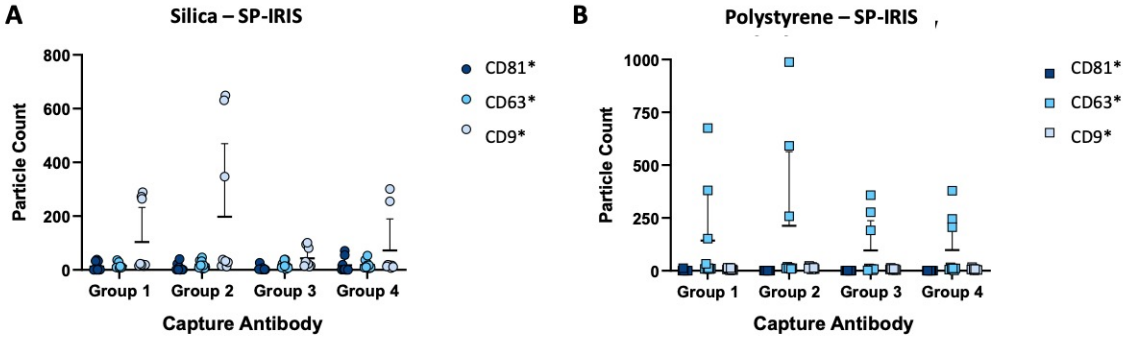


*Indicates target of fluorescent detection antibody

709

**Supplementary Figure 4. MRPS and NFCM dilution series**

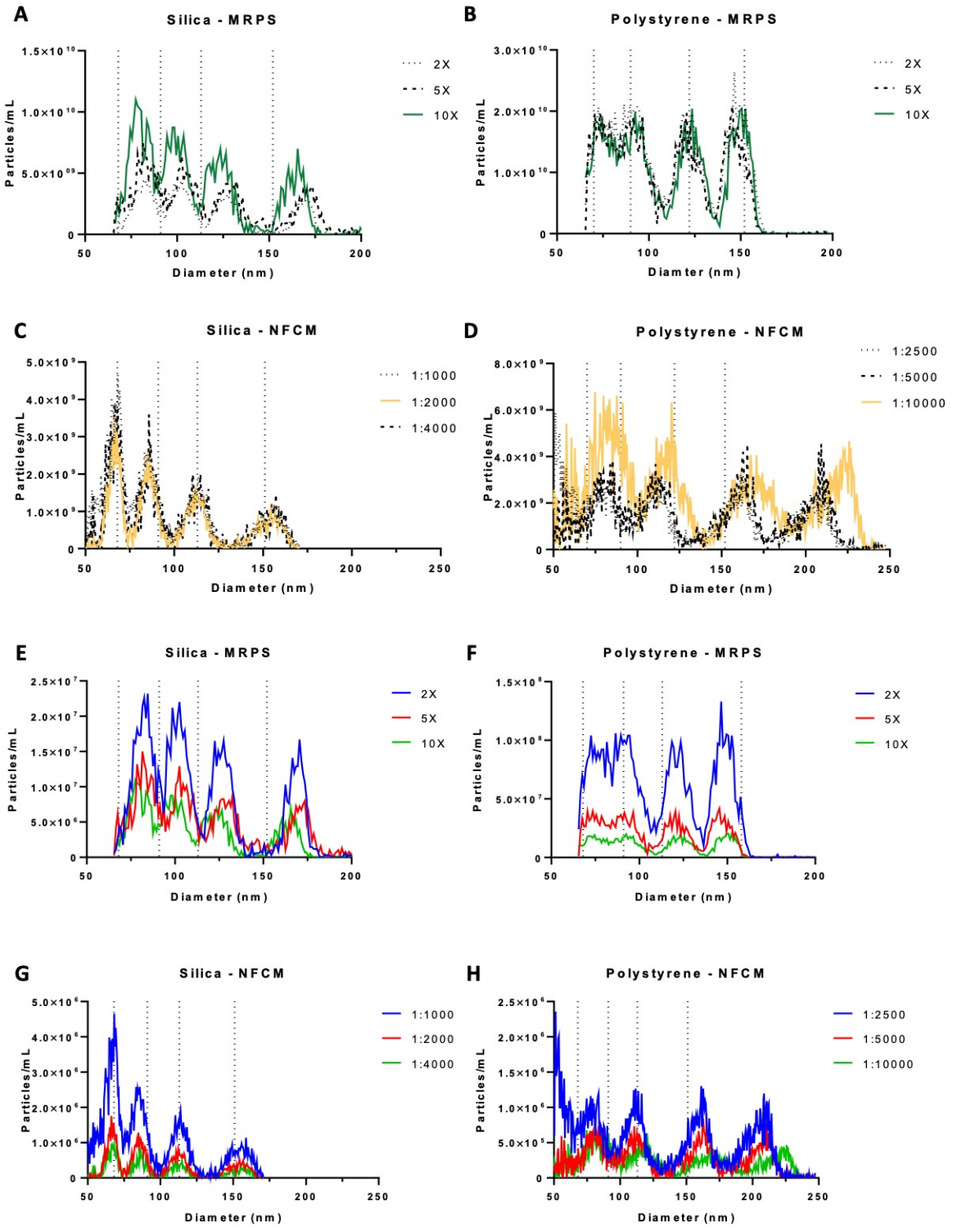


710

**Supplementary Table 1. Antibodies tested with fluorescent NTA**

| Tetraspanin | Fluorophore | Manufacturer | Catalog Number | Signal |
|---|---|---|---|---|
| CD81 | AF488 | Santa Cruz | sc-166029 | No |
| | PE | BD Biosciences | BDB555676 | Yes |
| | PerCP | BD Biosciences | BDB565430 | No |
| | APC | BD Biosciences | BDB561958 | No |
| CD63 | AF488 | Santa Cruz | sc-5275 | No |
| | AF488 | Novus Biologicals | NBP2-42225 | No |
| | PE | AbCam | ab205540 | No |
| | V450 | BD Biosciences | BDB561984 | No |
| CD9 | PE | BioLegend | 312106 | No |
| | PerCP | BD Biosciences | BDB561329 | No |
| | FITC | AbCam | ab34162 | No |

711